Electronic Supplementary Information

Pyrolysis of Cyano-Bridged Hetero-Metallic Aerogels: A General Route to Immobilize Sn–M (M=Fe, Ni) Alloys within Carbon Matrix for Stable and Fast Lithium Storage

*Hongxia Shi,† Anping Zhang,† Xiukui Zhang, Hemiao Yin, Siqi Wang, Yawen Tang, Yiming Zhou, Ping Wu**

Jiangsu Key Laboratory of New Power Batteries, Jiangsu Collaborative Innovation Center of Biomedical Functional Materials, School of Chemistry and Materials Science, Nanjing Normal University, Nanjing 210023, PR China.

*E-mail: zjuwuping@njnu.edu.cn (P.W.).

† Equal contribution to this work.

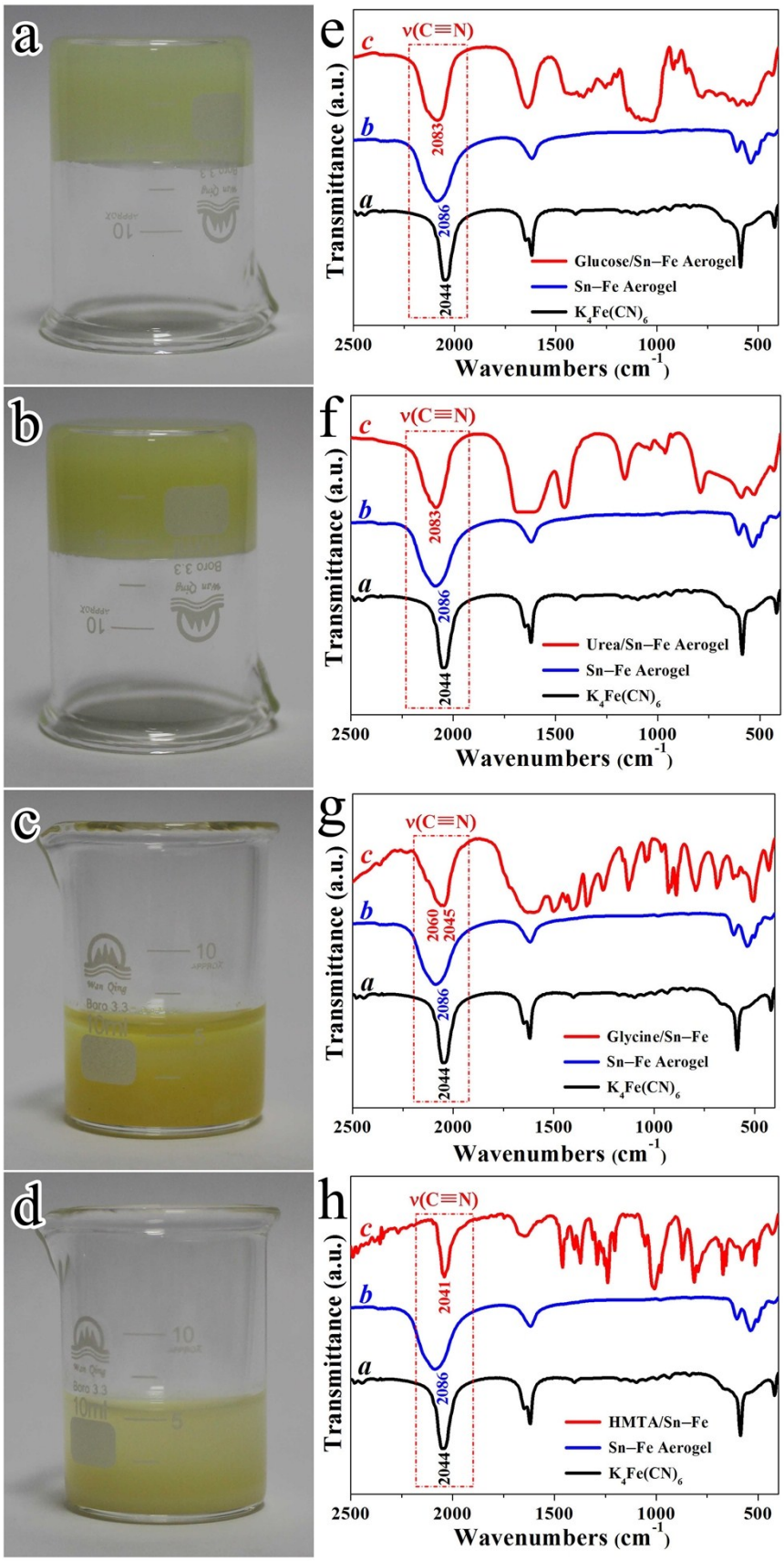

Fig. S1 Photographs of the glucose/Sn–Fe hydrogel (a), urea/Sn–Fe hydrogel (b), glycine/Sn–Fe suspension (c), HMTA/Sn–Fe suspension (d), and FTIR spectra of the glucose/Sn–Fe aerogel (e), urea/Sn–Fe aerogel (f), freeze-dried glycine/Sn–Fe (g) and HMTA/Sn–Fe (h) suspensions.

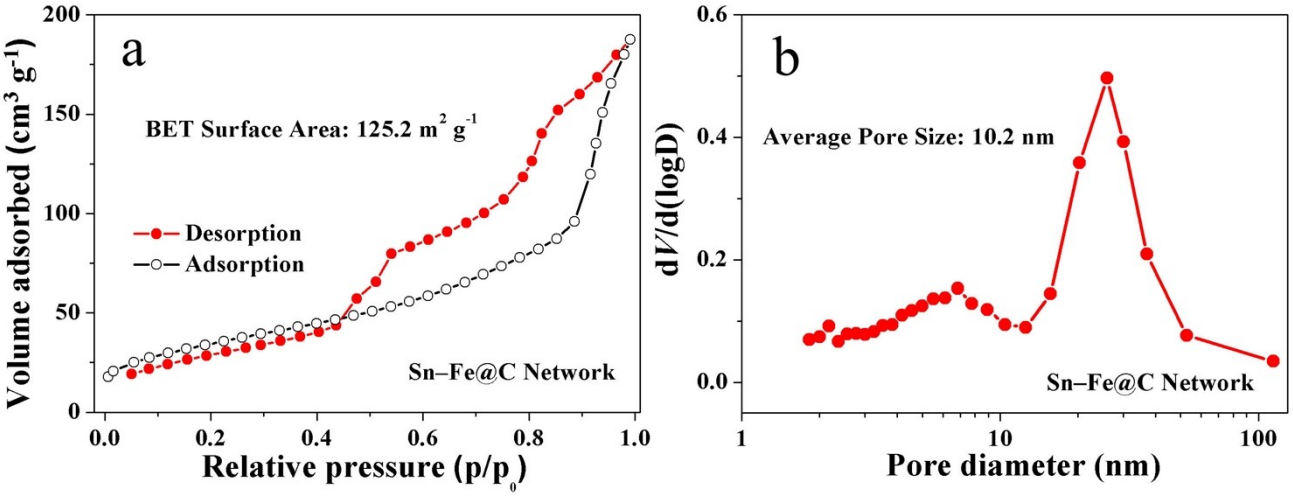

Fig. S2 Nitrogen adsorption/desorption isotherms (a) and pore size distribution (b) of the nanoporous Sn–Fe@C network.

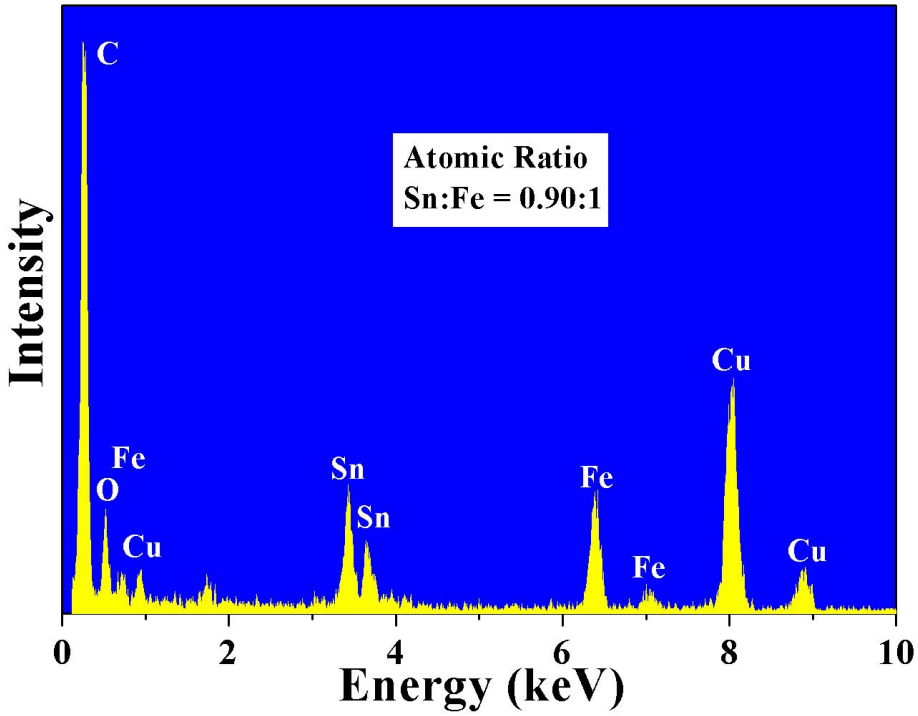

Fig. S3 EDS spectrum of the nanoporous Sn–Fe@C network.

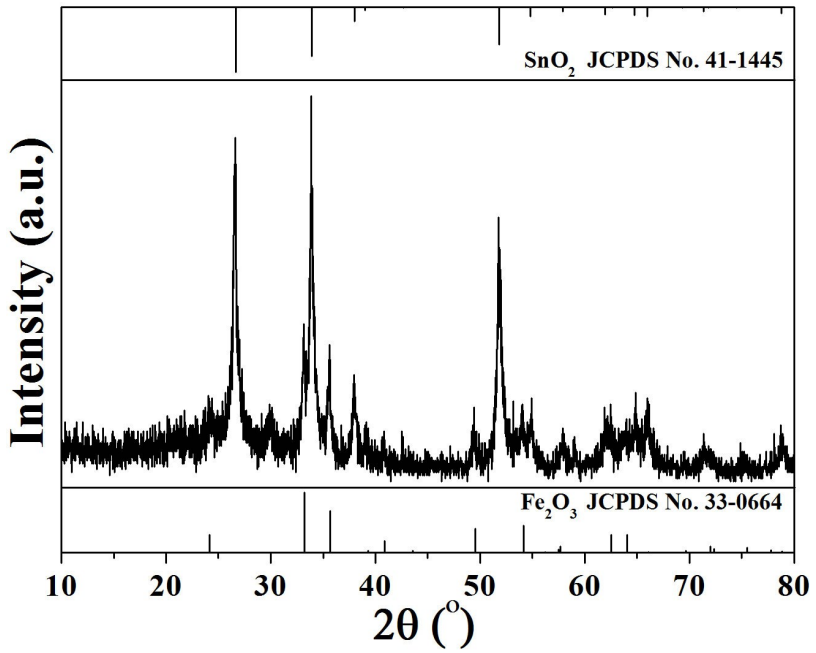

Fig. S4 XRD pattern of the nanoporous Sn–Fe@C network after TGA.

As seen from TGA curve (Fig. 5b), the weight variation of Sn–Fe@C network can be mainly attributed to the oxidation of Sn–Fe alloy and carbon components during TGA tests. The oxidation of Sn–Fe alloy leads to a weight increase, whereas the removal of carbon component leads to a weight decrease of the product. Fig. S4 shows the XRD pattern of the nanoporous Sn–Fe@C network after TGA. The observed crystalline phases from the oxidation product after TGA can be indexed to SnO_2 (JCPDS no. 41-1445) and Fe_2O_3 (JCPDS no. 33-0664). Additionally, the atomic ratio of Sn and Fe in the Sn–Fe alloy is determined to be 0.9:1 by EDS spectrum (Fig. S3), and thus the atomic ratio of SnO_2 and Fe_2O_3 in the oxidation product is 0.9:0.5. Therefore, the carbon content in the Sn–Fe@C network can be calculated based on the following equation:

$$\begin{aligned} C(wt\%) &= 100 - Sn\text{–}Fe(wt\%) \\ &= 100 - 100 \times \frac{\text{molecular weight of } (0.9Sn \text{ and } Fe)}{\text{molecular weight of } (0.9SnO_2 \text{ and } 0.5Fe_2O_3)} \times \frac{\text{final weight of } SnO_2 \text{ and } Fe_2O_3}{\text{initial weight of Sn–Fe@C network}} \end{aligned}$$

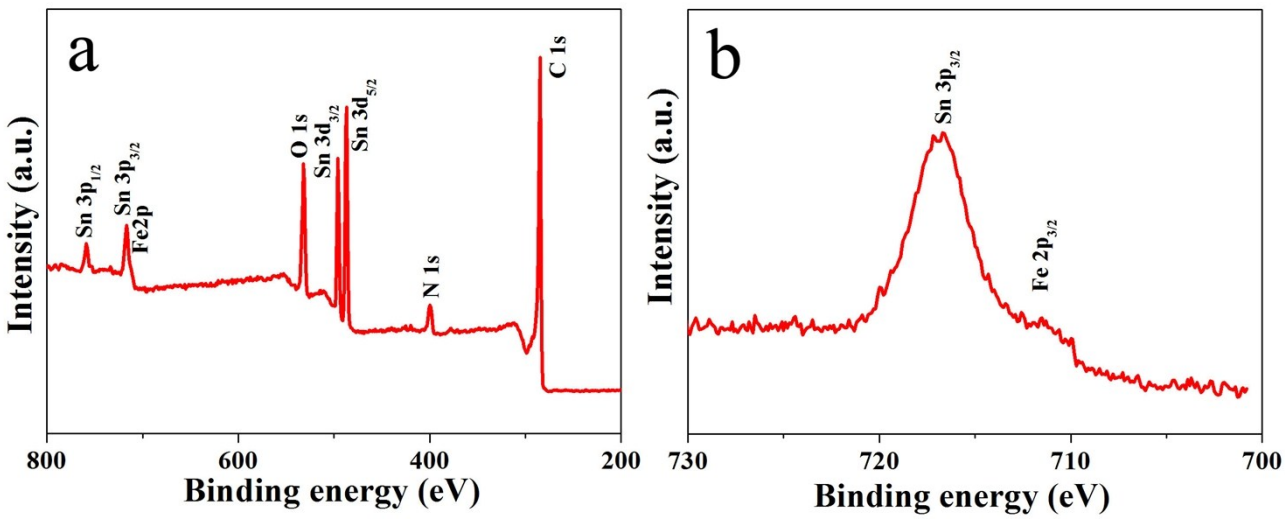

Fig. S5 XPS spectra of the nanoporous Sn–Fe@C network: (a) survey spectrum, and (b) Sn $3p_{3/2}$ and Fe $2p_{3/2}$ spectra.

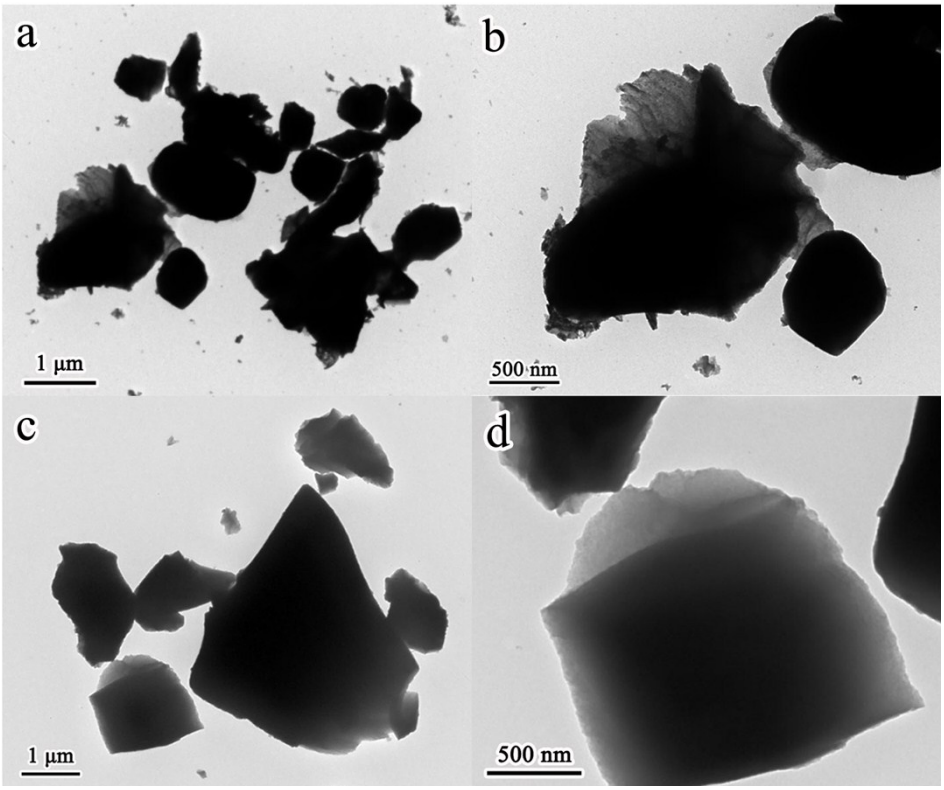

Fig. S6 TEM images of the Sn–Fe–C composite (a, b) and CA-derived carbon (c, d).

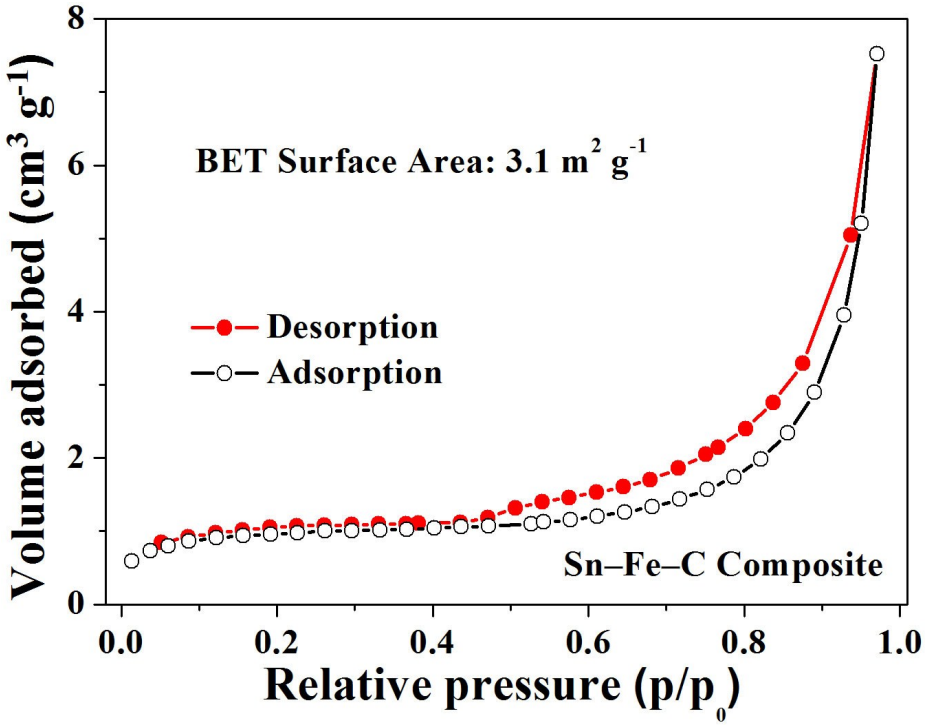

Fig. S7 Nitrogen adsorption/desorption isotherms of the Sn–Fe–C composite.

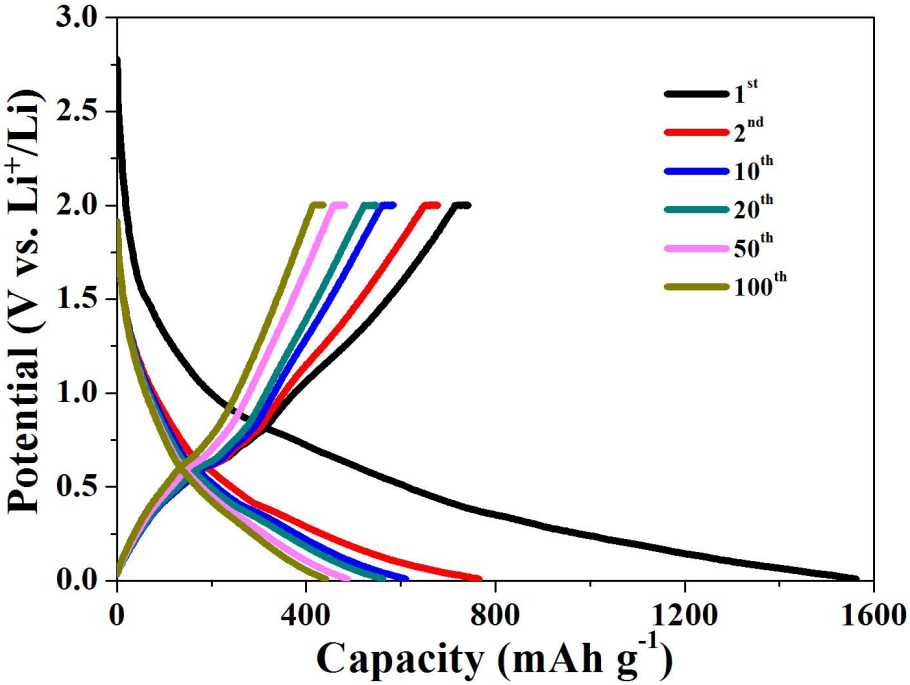

Fig. S8 The 1st, 2nd, 10th, 20th, 50th, and 100th discharge and charge curves of the nanoporous Sn–Fe@C network in the potential range of 0.01-2 V at a current density of 100 mA g^{-1}.

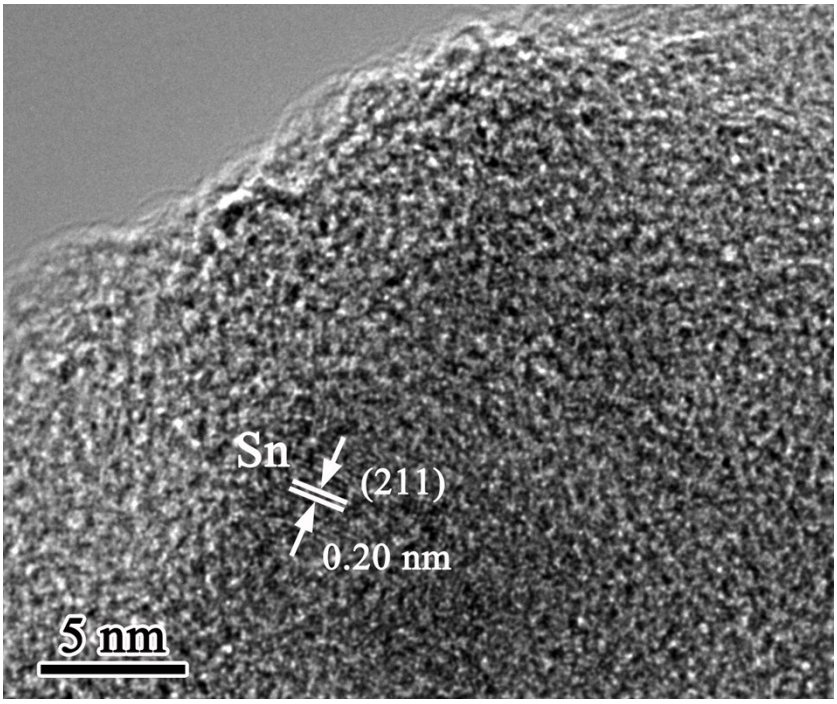

Fig. S9 HRTEM image of the nanoporous Sn–Fe@C network in a fully de-lithiated state (2.0 V *vs.* Li^+/Li) after 100 cycles.

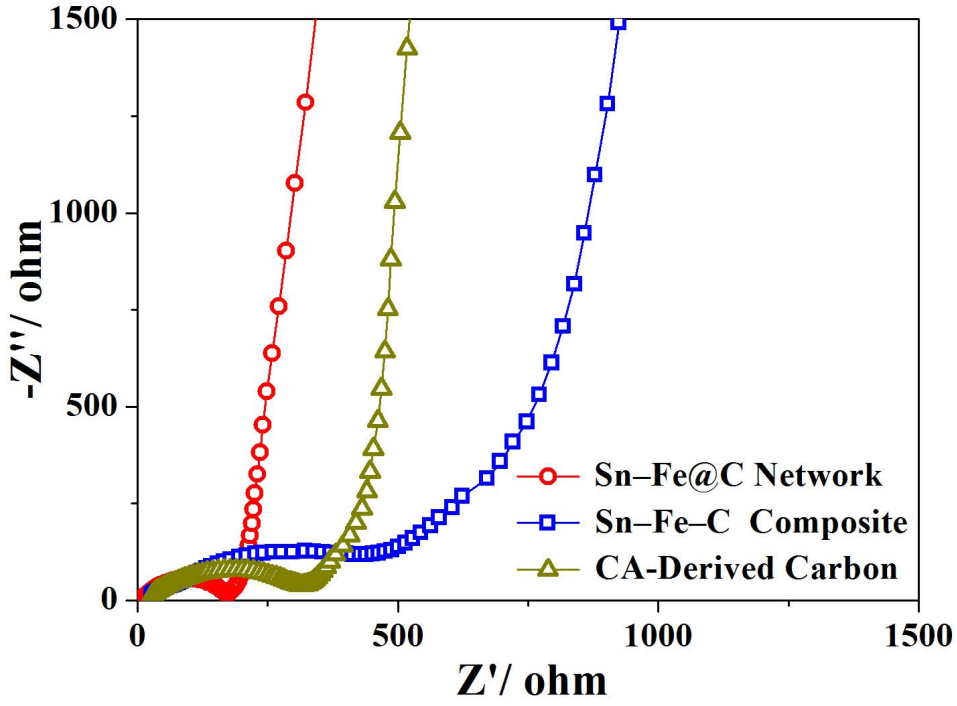

Fig. S10 Nyquist plots of the nanoporous Sn–Fe@C network in comparison with Sn–Fe–C composite and CA-derived carbon in fresh cells.

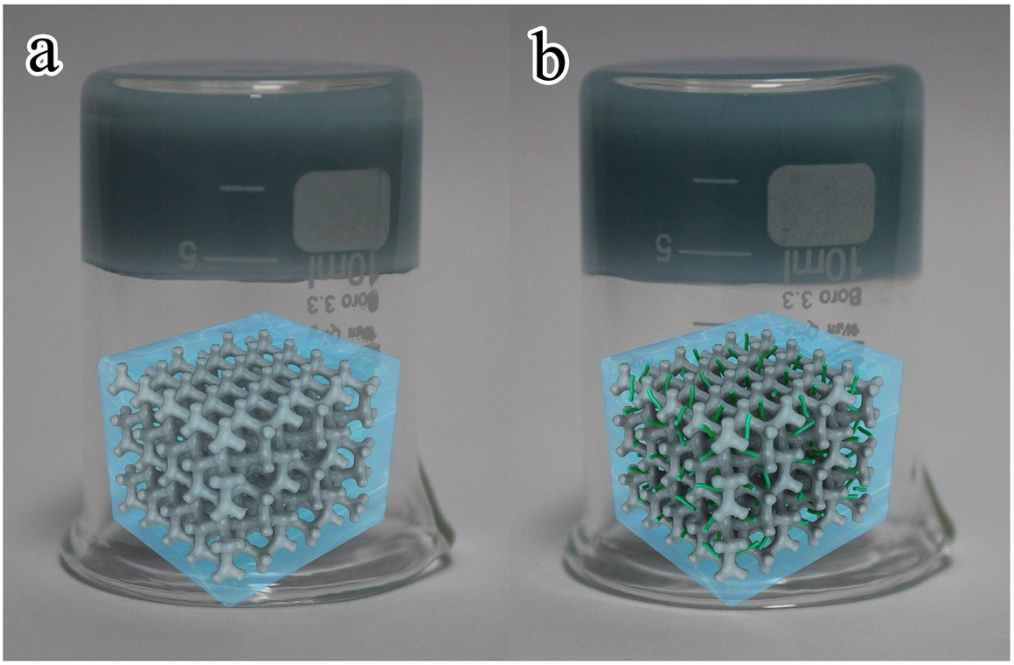

Fig. S11 Photographs of the cyano-bridged Sn–Ni hydrogel (a), CA/Sn–Ni hydrogel (b), and their corresponding models (*insets*).

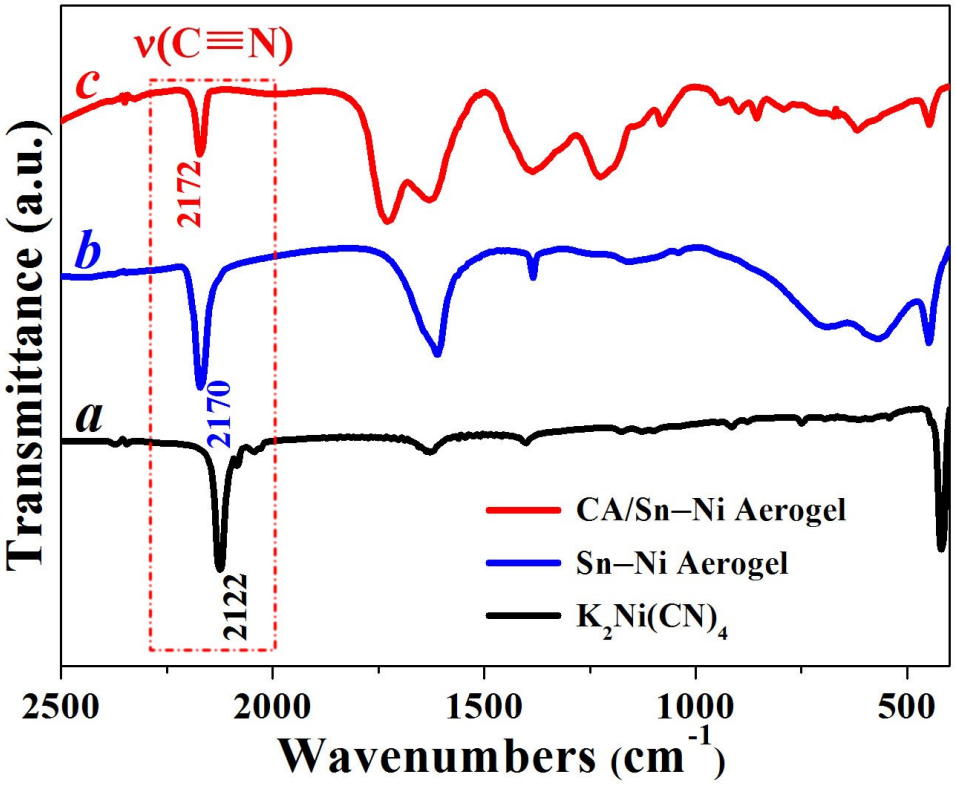

Fig. S12 FTIR spectra of the $K_2Ni(CN)_4$ reagent (curve *a*), cyano-bridged Sn–Ni aerogel (curve *b*), and CA/Sn–Ni aerogel (curve *c*).

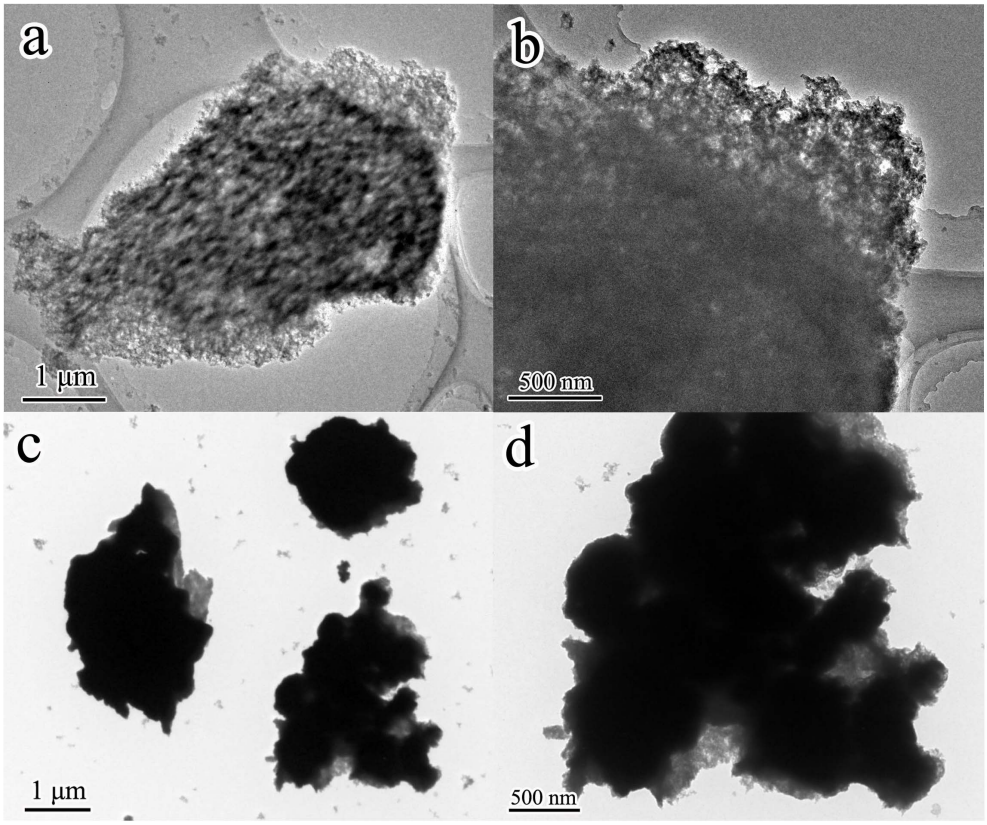

Fig. S13 TEM images of the nanoporous Sn–Ni@C network (a, b) and Sn–Ni–C composite (c, d).